Understanding the Ising zigzag antiferromagnetism of $FePS_3$ and $FePSe_3$ monolayers

Ke Yang,[1,2] Yueyue Ning,[1] Yuxuan Zhou,[2,3] Di Lu,[2,3] Yaozhenghang Ma,[2,3] Lu Liu,[2,3] Shengli Pu,[1] and Hua Wu[2,3,4,*]

[1]*College of Science, University of Shanghai for Science and Technology, Shanghai 200093, China*

[2]*Laboratory for Computational Physical Sciences (MOE), State Key Laboratory of Surface Physics, and Department of Physics, Fudan University, Shanghai 200433, China*

[3]*Shanghai Qi Zhi Institute, Shanghai 200232, China*

[4]*Shanghai Branch, Hefei National Laboratory, Shanghai 201315, China*

(Received 1 April 2024; revised 11 June 2024; accepted 11 July 2024; published 23 July 2024)

Transition metal phosphorous trichalcogenides represent a class of van der Waals magnetic materials ideal for exploring two-dimensional magnetism. This study investigates the spin-orbital states of $FePS_3$ and $FePSe_3$ monolayers and the origin of their Ising zigzag antiferromagnetism (AFM), using density functional calculations, crystal field level diagrams, superexchange analyses, and parallel tempering Monte Carlo (PTMC) simulations. Our calculations show that under the trigonal elongation of the FeS_6 ($FeSe_6$) octahedra, the e_g^π doublet of the Fe $3d$ crystal field levels lies lower than the a_{1g} singlet by about 108 meV (123 meV), which is much larger than the strength of Fe $3d$ spin-orbit coupling (SOC). Then, the half-filled minority-spin e_g^π doublet of the high-spin Fe^{2+} ions ($d^{5\uparrow,1\downarrow}$) splits by the SOC into the lower L_{z+} and higher L_{z-} states. The spin-orbital ground state $d^{5\uparrow}L_{z+}^{1\downarrow}$ formally with $S_z = 2$ and $L_z = 1$ gives the large z-axis spin/orbital moments of 3.51/0.76 μ_B (3.41/0.67 μ_B) for $FePS_3$ ($FePSe_3$) monolayer, and both the moments are reduced by the strong (stronger) Fe $3d$ hybridizations with S $3p$ (Se $4p$) states. As a result, $FePS_3$ ($FePSe_3$) monolayer has a huge perpendicular single-ion anisotropy (SIA) energy of 19.4 meV (14.9 meV), giving an Ising-type magnetism. Moreover, via the maximally localized Wannier functions, we find that the first-nearest-neighboring (1NN) Fe-Fe pair has large hopping parameters in-between some specific orbitals, and so does the third-nearest-neighboring (3NN) Fe-Fe pair. In contrast, the second-nearest-neighboring (2NN) Fe-Fe pair has much smaller hopping parameters and the fourth-nearest-neighboring Fe-Fe pair has negligibly small ones. Then, a combination of those hopping parameters and the superexchange picture can readily explain the computed strong 1NN ferromagnetic coupling and the strong 3NN antiferromagnetic one but the relatively much smaller 2NN antiferromagnetic coupling. Furthermore, our PTMC simulations give T_N of 119 K for $FePS_3$ monolayer and well reproduce its experimental Ising zigzag AFM, and also predict for $FePSe_3$ monolayer the same magnetic structure with a close or even higher T_N.

DOI: 10.1103/PhysRevB.110.024427

I. INTRODUCTION

The study of two-dimensional (2D) magnetic materials has seen a surge in interest [1–7] following the discovery of ferromagnetic (FM) behavior in the CrI_3 monolayer [8] and the $Cr_2Ge_2Te_6$ bilayer [9] in 2017. In line with the Mermin-Wagner theorem [10], the key to establishing magnetic order in 2D materials is magnetic anisotropy (MA). For instance, both the CrI_3 monolayer [8] and $Cr_2Ge_2Te_6$ bilayer [9] exhibit weak out-of-plane anisotropy due to the spin-orbit coupling (SOC) of heavy ligand p orbitals and their hybridization with closed Cr^{3+} t_{2g}^3 shell [11–14]. In stark contrast, the VI_3 monolayer exhibits giant single-ion anisotropy (SIA) of 16 meV per V atom associated with the open V^{3+} t_{2g}^2 shell and its SOC effects [15–17], and the experimental large orbital moment is 0.6 μ_B [18,19]. As the MA is essential to the 2D magnetism, it is desirable to have a large orbital moment, a giant SIA, and thus Ising-type magnetism [20–22].

Transition metal phosphorous trichalcogenides are a class of van der Waals layered materials, and among them, $FePS_3$ and $FePSe_3$ bulk materials are zigzag antiferromagnetic (AF) semiconductors [23–26] with close Néel temperatures (T_N) of 123 [27] and 119 K [23], respectively. Both compounds contain the Fe^{2+} ion with $S = 2$ and exhibit their respective effective magnetic moment of 5.23 μ_B for $FePS_3$ [27] and 4.90 μ_B for $FePSe_3$ [23]. Note that taking into account a covalent reduction, a spin-only $S = 2$ state would have the effective magnetic moment less than 4.9 μ_B ($\sqrt{g_s^2 S(S+1)} = \sqrt{2^2 \times 2 \times 3} \approx 4.9$). Therefore, the above effective moments larger than or equal to 4.9 μ_B imply a contribution of additional orbital moments [27].

Recently, $FePS_3$ has been successfully exfoliated to a monolayer, which maintains the zigzag AF ordering with $T_N = 118$ K [24,28,29]. This T_N remains almost independent of thickness, from bulk to the monolayer limit, indicating the predominance of a strong Ising-type magnetism [24]. Several theoretical works [30–35] have confirmed the zigzag AF ground state, showing a strong first-nearest-neighboring (1NN) FM coupling and a strong

*Contact author: wuh@fudan.edu.cn

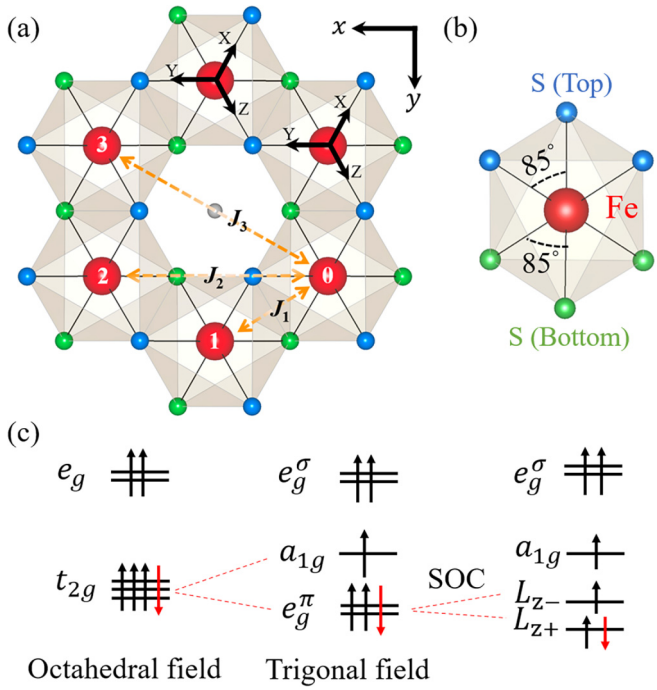

FIG. 1. (a) The atomic structure of $FeP X_3$ (X = S, Se) monolayer, with the P-P dimer located vertically across the center of the honeycomb formed by Fe ions, and (b) the edge-shared FeX_6 (X = S, Se) octahedron. (c) The Fe^{2+} $3d^6$ spin-orbital states with $S = 2$ in the local octahedral but global trigonal crystal field.

third-nearest-neighboring (3NN) AF one but a much smaller second-nearest-neighboring (2NN) AF coupling. So far, the Ising magnetism has been confirmed [24,27,33], however, the corresponding electronic structure and spin-orbital state remain less clear. Therefore, here we provide an insight into the Ising magnetism of $FePS_3$ and $FePSe_3$ monolayers. Moreover, we use the iNN (i = 1–4) hopping parameters, derived from the Wannier functions, to explain the competitive 1NN FM and 3NN AF couplings in determining the zigzag AFM. Then, our parallel tempering Monte Carlo (PTMC) simulations yield a rational T_N value.

In $FePS_3$ and $FePSe_3$ monolayers, Fe^{2+} ions in the local octahedral coordination are influenced by the global trigonal crystal field (see Fig. 1). This field splits the t_{2g} triplet into a higher a_{1g} singlet and a lower e_g^π doublet due to the elongation of the octahedra along the global z axis, as illustrated in Figs. 1(b) and 1(c). The crystal field splitting between the a_{1g} singlet and e_g^π doublet is calculated to be 108 (123) meV for $FePS_3$ ($FePSe_3$) as seen below. After a direct comparison of different spin-orbital states in the following calculations, we find the $3d^{5\uparrow}L_{z+}^{1\downarrow}$ ground state with the formal $S_z = 2$ and $L_z = 1$, as seen in Fig. 1(c). Then, the consequent big perpendicular orbital moment and huge SIA readily account for the experimental Ising magnetism. Moreover, this work consistently explains the Ising-type zigzag AFM of $FePS_3$ and $FePSe_3$ monolayers, using the first-principles calculations of their spin-orbital states and the superexchange parameters, the hopping parameters derived from Wannier functions, and the PTMC simulations. Furthermore, we predict that their T_N would be enhanced under a compressive strain.

II. COMPUTATIONAL DETAILS

Density functional theory (DFT) calculations are performed using the Vienna *ab initio* simulation package (VASP) [36]. The generalized gradient approximation (GGA) proposed by Perdew, Burke, and Ernzerhof (PBE) [37] is used to describe the exchange-correlation potential. The optimized lattice constants $a = b = 5.93$ (6.28) Å for $FePS_3$ ($FePSe_3$) monolayer are close to the experimental bulk values of 5.95 [38] (6.27 [23]) Å. A 20-Å-thick slab is used to model $FeP X_3$ (X = S, Se) monolayer. The kinetic energy cutoff is set to 450 eV. The total energies and atomic forces converge to 10^{-5} eV and 0.01 eV/Å. A Monkhorst-Pack k mesh of $6 \times 6 \times 1$ ($6 \times 3 \times 1$) is used for 1×1 unit cell ($1 \times \sqrt{3}$ supercell). The setup of kinetic energy and k-point sampling is carefully tested, as seen in Table S1 in Supplemental Material (SM) [39].

To describe the correlation effect of the localized Fe $3d$ electrons, we employ the GGA + U approach [40]. The Hubbard U values are calculated, through the constrained random phase approximation [41], to be 3.6 eV for $FePS_3$ monolayer and 2.7 eV for $FePSe_3$, with the common value of Hund's exchange $J_H = 0.9$ eV. Both the U and J_H are included in the following GGA + U + J_H (normally referred to as GGA + U) calculations. The reduction of the U values from $FePS_3$ to $FePSe_3$ could mainly be due to an enhanced Coulomb screening effect resulting from a stronger Fe $3d$-Se $4p$ hybridization. Moreover, the stronger Fe $3d$-Se $4p$ hybridizations will affect the hopping integrals and superexchange, as seen in Sec. III E. Note that J_H is actually the difference of the energies of electrons with different spins or orbitals on the same atomic shell and, therefore, J_H is almost not screened and not modified when going from an atom to a solid. It is almost a constant for a given element and is typically 0.8–1.0 eV for a $3d$ transition metal [42]. We also test the common $U = 4$ eV for both $FePS_3$ and $FePSe_3$ monolayers (see Table S2 and Fig. S1 in SM [39]) and find that some quantitative change of the results does not affect our conclusions. To figure out the ground state among a set of spin-orbital states, the occupation number matrices

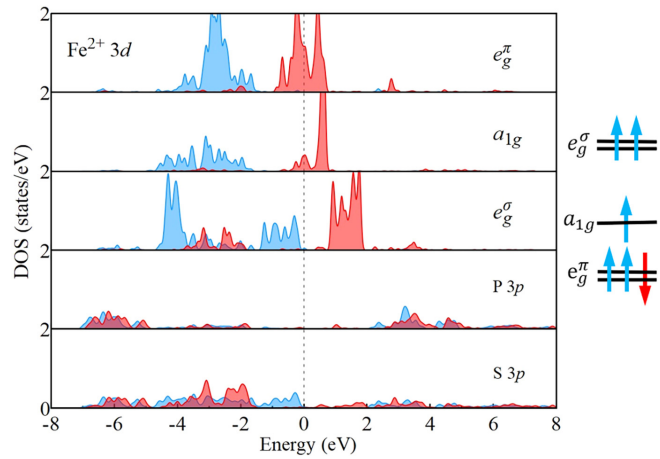

FIG. 2. Density of states (DOS) of $FePS_3$ monolayer by GGA calculation. The Fermi level is set at zero energy. The blue (red) curves stand for the up- (down-) spin channel.

are controlled in our calculations using the open-source software developed by Watson [43]. The SOC is included in our calculations using the second-variational method with scalar relativistic wave functions.

The hopping parameters are obtained from maximally localized Wannier functions (MLWFs) using the WANNIER90 [44,45]. Moreover, we perform PTMC [46] simulations to estimate the T_N of $FePS_3$ and $FePSe_3$ monolayers on a $12 \times 12 \times 1$ spin matrix with periodic boundary conditions, and the number of replicas is set to 112. A similar result is obtained with larger supercells. During the simulation step, each spin is rotated randomly in the three-dimensional space. The spin dynamical process is studied by the classical Metropolis methods [47].

We adopt the global coordinate system with the z axis along the local [111] direction of the FeX_6 (X = S, Se) octahedra [see Fig. 1(a) for the local XYZ axes and global xyz axes]. The eigenwave function in the local octahedral but global trigonal crystal field, under the global xyz coordinate system, can be expressed as

$$
\begin{aligned}
|a_{1g}\rangle &= |3z^2 - r^2\rangle, \\
|e^{\pi}_{g_1}\rangle &= \sqrt{\frac{2}{3}}|x^2 - y^2\rangle - \sqrt{\frac{1}{3}}|xz\rangle, \\
|e^{\pi}_{g_2}\rangle &= \sqrt{\frac{1}{3}}|yz\rangle + \sqrt{\frac{2}{3}}|xy\rangle, \\
|e^{\sigma}_{g_1}\rangle &= \sqrt{\frac{1}{3}}|x^2 - y^2\rangle + \sqrt{\frac{2}{3}}|xz\rangle, \\
|e^{\sigma}_{g_2}\rangle &= \sqrt{\frac{2}{3}}|yz\rangle - \sqrt{\frac{1}{3}}|xy\rangle. \qquad (1)
\end{aligned}
$$

Considering the crystal field splitting and SOC effect, the half-filled down-spin e^{π}_g doublet of the Fe^{2+} $3d^6$ high-spin state would carry an unquenched orbital moment characterized by the effective orbital momentum $L = 1$ [see Fig. 1(c)]. Their eigenwave functions are expressed as

$$
|L_{z\pm}\rangle = \frac{1}{\sqrt{2}}\left(|e^{\pi}_{g_1}\rangle \pm i|e^{\pi}_{g_2}\rangle\right), \qquad (2)
$$

where L_z represents the projection of orbital moment along the z axis, and $\pm$ stands for the $L_z = \pm 1$.

III. RESULTS AND DISCUSSION

A. The Fe^{2+} high-spin $S = 2$ state

We initially focus on $FePS_3$ monolayer, for which experimental results are available for comparison [24,28,29]. To see the crystal field effect, exchange splitting, electron correlation, and the crucial SOC effects, we present and discuss below the spin-polarized GGA and GGA + SOC + U calculations. First, we perform spin-polarized GGA calculations for the FM state to investigate the crystal field effect and the charge-spin state of the $FePS_3$ monolayer. As shown in Fig. 2, the octahedral t_{2g}-e_g crystal field splitting is about 1 eV in good agreement with the experiment [48], and in the global trigonal crystal field, the t_{2g} triplet further splits into the a_{1g} singlet and e^{π}_g doublet. The five up-spin $3d$ orbitals are fully occupied, while the down-spin e^{π}_g doublet is half-filled, leading to the Fe^{2+} $3d^{5\uparrow}(e^{\pi}_g)^{1\downarrow}$ configuration. In comparison with the Fe $3d$ orbitals around the Fermi level, however, the P $3p$ orbitals have little contribution around the Fermi level. Instead, there is a large bonding-antibonding split (about –6 eV vs 3 eV both relative to the Fermi level), which arises from the P-P dimerization. In contrast, the S $3p$ states have strong hybridization with Fe $3d$ orbitals, and they have a large and broad contribution in the energy range from –6 eV to the Fermi level. Therefore, it is undoubted that the S $3p$ states would play a vital role in the superexchange interactions mediating the magnetic couplings in the Fe sublattice.

Moreover, $FePS_3$ monolayer exhibits a total spin moment of 3.97 μ_B/f.u. for the FM state, suggesting the formal Fe^{2+} $S = 2$ high-spin state. The Fe^{2+} ion displays a local spin moment of 3.37 μ_B. Owing to the Fe $3d$-S $3p$ hybridization, each sulfur ion gets spin polarized and has a local spin moment of 0.11 μ_B, and an additional spin moment of 0.28 μ_B/f.u. appears in the interstitial region. To confirm the high-spin $S = 2$ ground state of the Fe^{2+} ion, we also compute the low-spin $S = 0$ state and find it to be 796 meV/f.u. unstable against the high-spin ground state. Note that it is the magnitude of the t_{2g}-e_g octahedral crystal field splitting (Δ_{cf}) relative to J_H which determines the spin state of the Fe^{2+} ion. To make a crude estimate: the $S = 2$ state ($3d^{5\uparrow}t^{1\downarrow}_{2g}$) carries the Hund's coupling energy of $-10J_H$ plus $2\Delta_{cf}$ (the crystal field excitation energy of two electrons on the e_g orbitals), whereas the $S = 0$ state ($t^{3\uparrow 3\downarrow}_{2g}$) has a total stabilization energy of $-6J_H$. Therefore, a critical value for a high-spin to low-spin transition is $\Delta_{cf} > 2J_H = 1.8$ eV. As seen in Fig. 2, the t_{2g}-e_g crystal field splitting Δ_{cf} is about 1 eV and much smaller than the critical value of 1.8 eV. Therefore, $FePS_3$ monolayer is well stabilized in the high-spin $S = 2$ ground state.

As seen above, $FePS_3$ monolayer exhibits the Fe^{2+} $3d^{5\uparrow}(e^{\pi}_g)^{1\downarrow}$ high-spin state. The e^{π}_g doublet has a lower crystal field energy than the a_{1g} singlet, which accords with the elongation of the FeS_6 octahedra along the z axis as depicted in Fig. 1(b), where the marked S-Fe-S bond angles of 85° deviate from the ideal ones of 90°. As a result, the a_{1g} singlet rises up in the crystal field energy. As seen below, the half-filling of the down-spin e^{π}_g doublet is crucial for the Ising magnetism of $FePS_3$. When the SOC is included ($\zeta \vec{l} \cdot \vec{s}$), the e^{π}_g doublet would split into the $L_{z+} = +1$ and $L_{z-} = -1$ states as expressed in Eq. (2).

B. The $L_z = 1$ ground state and Ising magnetism

Then, to investigate the effects of SOC and electron correlation, we perform GGA + SOC + U calculations. The obtained insulating solution has a total spin moment of 4 μ_B/f.u. for the FM state and a local spin moment of 3.55 μ_B for the Fe ion, reinforcing the formal Fe^{2+} $S = 2$ state. Additionally, we observe a large orbital moment of 0.73 μ_B on the Fe^{2+} ion, in line with the splitting of the e^{π}_g doublet due to SOC, resulting in the $3d^{5\uparrow}L^{1\downarrow}_{z+}$ configuration. As depicted in Fig. 3(a), the five up-spin $3d$ orbitals are fully occupied. The single down-spin electron occupies the lower-energy L_{z+} orbital, leaving the higher-energy L_{z-} orbital empty, resulting in a semiconductor with a band gap of 0.7 eV. This leads to the $3d^{5\uparrow}L^{1\downarrow}_{z+}$ state with a large orbital moment along the z axis.

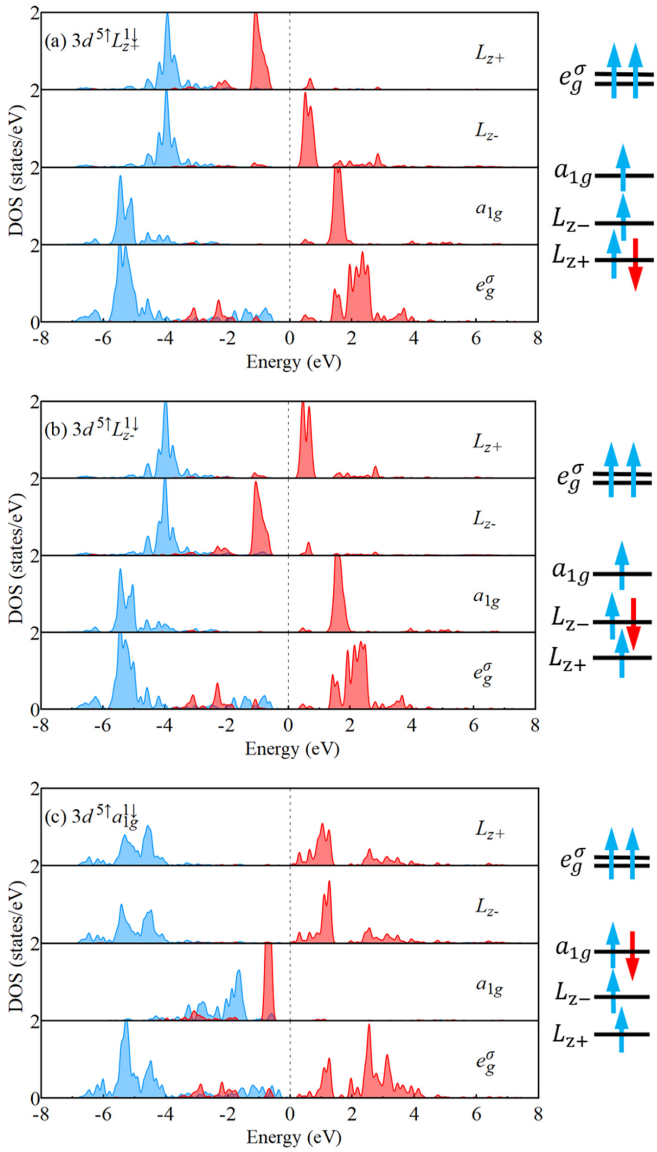

FIG. 3. The DOS results of $FePS_3$ monolayer in (a) the $3d^5\uparrow L_{z+}^{1\downarrow}$ ground state, (b) $3d^5\uparrow L_{z-}^{1\downarrow}$, and (c) $3d^5\uparrow a_{1g}^{1\downarrow}$ states by the GGA + SOC + U calculations, and the corresponding crystal field level diagrams. The blue (red) curves stand for the up- (down-) spin channel. The Fermi level is set at zero energy.

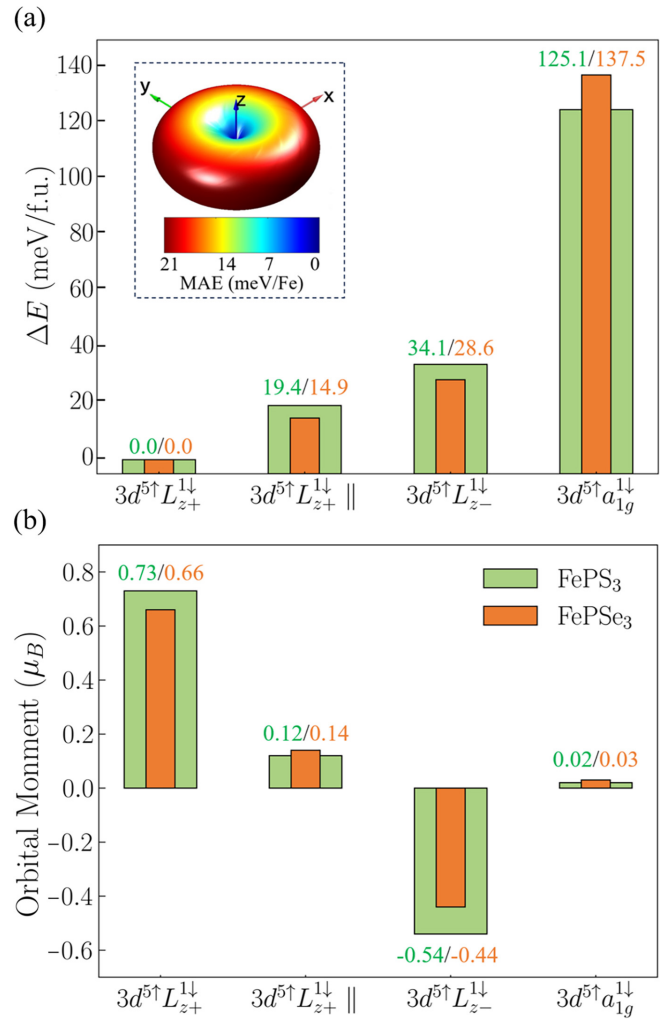

FIG. 4. (a) The relative total energies ΔE (meV/f.u.), and (b) orbital moments for $FePS_3$ and $FePSe_3$ monolayers in different spin-orbital states by GGA + SOC + U calculations. The symbol || in the state labeling marks the in-plane magnetization, in comparison with other states with out-of-plane magnetization.

The band gap of 0.7 eV between the occupied L_{z+} and unoccupied L_{z-} states is mainly due to the electron correlation effect, and it significantly exceeds the typical SOC effect. To evaluate the spin-orbital excitation energy such as the L_{z+}/L_{z-} orbital splitting by SOC, we focus on the computed total-energy differences between the $3d^5\uparrow L_{z+}^{1\downarrow}$ and $3d^5\uparrow L_{z-}^{1\downarrow}$ configurations, other than relying on the DOS results. For this assessment, we perform GGA + SOC + U calculations, enabling a direct comparison between these configurations, initialized via the occupation density matrix over the eigenorbitals.

As depicted in Fig. 3(b), the Fe^{2+} five up-spin $3d$ orbitals are fully occupied, and the single down-spin electron occupies the L_{z-} orbital, forming the $3d^5\uparrow L_{z-}^{1\downarrow}$ spin-orbital state. The Fe^{2+} ion now has a local spin moment of 3.54 μ_B and, notably, it exhibits an opposite orbital moment of -0.54 μ_B (see the results in Fig. 4). In the $3d^5\uparrow L_{z-}^{1\downarrow}$ state, the up-spin subshell is closed, and the single down-spin electron unfavorably carries a parallel negative orbital moment. As a result, the $3d^5\uparrow L_{z-}^{1\downarrow}$ state rises in the SOC energy against the $3d^5\uparrow L_{z+}^{1\downarrow}$ state by $\Delta E_{SOC} = \zeta(\Delta l_z)s_z = \zeta(0.73 + 0.54) \times 1/2$, which is 34.1 meV/f.u. as seen in Fig. 4. Then, here the SOC parameter ζ is estimated to be 53.7 meV. As the ζ parameter for the Fe^{2+} ion is typically around 50–60 meV, the present agreement reflects the good accuracy of our calculations.

When studying the SOC effect, it is important to compare the SOC with the crystal field splitting. As the e_g-t_{2g} crystal field splitting of about 1 eV is one order of magnitude stronger than the SOC, the e_g doublet is irrelevant when dealing with the SOC. The a_{1g}-e_g^π splitting within the t_{2g} triplet is thus of concern. For this purpose, we also stabilize the $3d^5\uparrow a_{1g}^{1\downarrow}$ state in our calculations [see Fig. 3(c)], and then compare it with the above $3d^5\uparrow L_{z+}^{1\downarrow}$ state. Owing to the singlet nature of the

a_{1g} orbital, the $3d^{5\uparrow}a_{1g}^{1\downarrow}$ state has only a tiny orbital moment of 0.02 μ_B, in addition to the Fe^{2+} spin moment of 3.51 μ_B. Our results show that the $3d^{5\uparrow}a_{1g}^{1\downarrow}$ state lies above the $3d^{5\uparrow}L_{z+}^{1\downarrow}$ state by $\Delta E = 125.1$ meV/f.u. (see Fig. 4), and this value is close to the experimental one of about 120 meV [48]. Then the a_{1g}-e_g^π trigonal crystal field splitting can be estimated to be $\Delta E - \frac{1}{2}\Delta E_{SOC} = 125.1 - \frac{1}{2} \times 34.1 = 108$ meV. This a_{1g}-e_g^π splitting is nearly three (two) times as large as the ΔE_{SOC} of 34.1 meV (the ζ parameter 53.7 meV) and, therefore, the a_{1g}-e_g^π mixing by the SOC is insignificant, and then we could restrict our discussion of the SOC effect within the half-filled down-spin e_g^π doublet as seen above.

Through the above calculations of the different spin-orbital states, we find that $FePS_3$ monolayer lies in the $3d^{5\uparrow}L_{z+}^{1\downarrow}$ ground state and carries the high-spin moment of 3.55 μ_B and a big orbital moment of 0.73 μ_B along the z axis. Owing to the SOC coupling, the spin moment is also fixed along the z axis. If the spin moment was rotated into the xy plane, only a small in-plane orbital moment of 0.12 μ_B would appear, and then the SOC energy would be largely lost and this state has a higher total energy than the $3d^{5\uparrow}L_{z+}^{1\downarrow}$ ground-state solution by 19.4 meV/Fe (see Fig. 4). As a result, this significant SIA defines the huge perpendicular magnetic anisotropy energy (MAE) of 19.4 meV/Fe, which is two or three orders of magnitude stronger than the MAE in CrI_3 monolayer [12–14,16]. Therefore, $FePS_3$ displays the robust Ising magnetism as experimentally observed [24,28,29].

C. The origin of the zigzag AFM

$FePS_3$ monolayer possesses the $3d^{5\uparrow}L_{z+}^{1\downarrow}$ spin-orbital ground state with $S_z = 2$ and $L_z = 1$. Based on this strong Ising magnetic spin-orbital state, we investigate the experimentally observed zigzag AFM [24,28,29]. We conduct calculations for three AF states, zigzag AF, Néel AF, and stripe AF, in addition to the FM state. These states are illustrated in Fig. 5, using a $1 \times \sqrt{3}$ supercell. Our results indicate that the zigzag AF state is most favorable (with a band gap of 1.2 eV, not shown) and exhibits the lowest total energy compared to the other three magnetic states by 17.1–36.7 meV/f.u., as shown in Table I. This result confirms the experimentally observed zigzag AFM [24,28,29]. To seek the origin of the zigzag AF ground state, we identify three exchange parameters: 1NN Fe_0-Fe_1 (J_1), 2NN Fe_0-Fe_2 (J_2), and 3NN Fe_0-Fe_3 (J_3), as seen in Fig. 5. Considering the magnetic exchange expression $-JS^2$ (FM for $J > 0$) for each pair of Fe^{2+} $S = 2$ ions, we calculate the relative energies per formula unit of $FePS_3$ monolayer in the four magnetic structures:

$$E_{\text{zigzag AF}} = \left(-\frac{1}{2}J_1 + J_2 + \frac{3}{2}J_3\right)S^2,$$
$$E_{\text{FM}} = \left(-\frac{3}{2}J_1 - 3J_2 - \frac{3}{2}J_3\right)S^2,$$
$$E_{\text{Néel AF}} = \left(+\frac{3}{2}J_1 - 3J_2 + \frac{3}{2}J_3\right)S^2,$$
$$E_{\text{stripe AF}} = \left(+\frac{1}{2}J_1 + J_2 - \frac{3}{2}J_3\right)S^2. \quad (3)$$

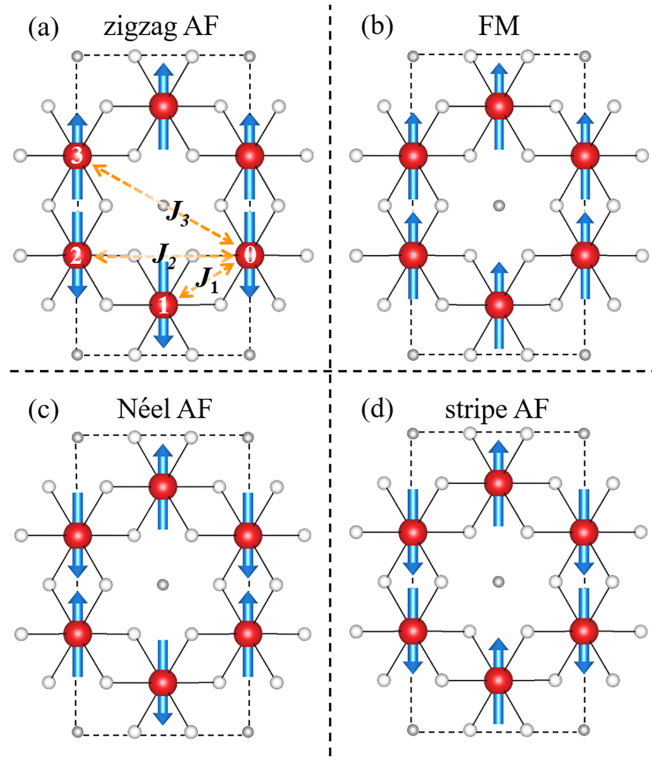

FIG. 5. The four magnetic structures of $FePS_3$ monolayer marked with three exchange parameters.

Using the relative total energies in Table I and applying Eq. (3), we determine the exchange parameters for $FePS_3$ monolayer as $J_1 = 3.13$ meV, $J_2 = -0.34$ meV, and $J_3 = -2.01$ meV. Our results indicate that the 1NN Fe^{2+} ions, separated by 3.42 Å, have a strong FM coupling, while the 2NN, at a distance of 5.93 Å, exhibits a much weaker AF coupling. Intriguingly, the 3NN J_3 Fe^{2+} ions, situated 6.84 Å apart, twice the 1NN distance, manifest a strong AF coupling. These results closely match the experimental ones from magnon

TABLE I. Relative total energies ΔE (meV/f.u.), local spin and orbital moments (μ_B), and the derived three exchange parameters (meV) for $FePS_3$ and $FePSe_3$ monolayers by the GGA + SOC + U calculations.

Systems	States	ΔE	Fe_{spin}	Fe_{orb}
$FePS_3$	Zigzag AF	0	±3.51	±0.76
	FM	17.1	3.55	0.73
	Néel AF	30.5	±3.49	±0.85
	Stripe AF	36.7	±3.52	±0.78
	$J_1 = 3.13$		$J_2 = -0.34$	$J_3 = -2.01$
$FePSe_3$	Zigzag AF	0	±3.41	±0.67
	FM	29.7	3.46	0.66
	Néel AF	42.4	±3.38	±0.83
	Stripe AF	43.7	±3.41	±0.69
	$J_1 = 3.53$		$J_2 = -0.89$	$J_3 = -2.47$

TABLE II. The hopping parameters (meV) of 1NN Fe_0-Fe_1, 2NN Fe_0-Fe_2, 3NN Fe_0-Fe_3, and 4NN Fe_0-Fe_4 in $FePS_3$ monolayer.

Hopping (t)		Fe_0				
		$3Z^2$-R^2	X^2-Y^2	XY	XZ	YZ
Fe_1	$3Z^2$-R^2	–64	0	79	6	5
	X^2-Y^2	0	–71	0	23	–23
	XY	79	0	–277	29	29
	XZ	6	23	29	74	–43
	YZ	5	–23	29	–43	73
Fe_2	$3Z^2$-R^2	1	25	7	–38	16
	X^2-Y^2	7	19	27	–42	–6
	XY	–13	11	18	–7	–11
	XZ	–17	–54	15	0	–7
	YZ	21	19	–15	15	18
Fe_3	$3Z^2$-R^2	140	99	3	–4	–27
	X^2-Y^2	99	26	2	–2	47
	XY	3	2	6	–13	–3
	XZ	–4	–2	–13	6	–2
	YZ	–27	47	–3	–2	–37
Fe_4	$3Z^2$-R^2	9	0	1	–5	4
	X^2-Y^2	0	–2	–1	–5	5
	XY	1	–1	4	–2	–1
	XZ	–5	–5	–2	–3	9
	YZ	4	5	–1	9	7

bands measurement [49]. The interplay of 1NN FM and the long-range AF interactions of 3NN is crucial to the zigzag AF ground state observed in $FePS_3$ monolayer [24,28,29].

Here, we provide an insight into the 1NN FM coupling, the much weaker 2NN AF coupling, and the strong 3NN AF coupling, by examining the relevant hopping parameters through Wannier function analyses. Given the honeycomb lattice of the Fe^{2+} magnetic ions and the edge-sharing FeS_6 octahedral network [see Fig. 1(a)], here we adopt a local octahedral XYZ coordinate system, where the XYZ axes are directed from Fe to neighboring S (Se) ions. The eigenwave functions of the local octahedral structure under a trigonal crystal field can be described as

$$|e^{\sigma}_{g_{1,2}}\rangle = \frac{1}{\sqrt{2}}(|3Z^2 - R^2\rangle \pm |X^2 - Y^2\rangle),$$
$$|a_{1g}\rangle = \frac{1}{\sqrt{3}}(|XY\rangle + |XZ\rangle + |YZ\rangle),$$
$$|L_{z\pm}\rangle = \frac{1}{\sqrt{3}}(|XY\rangle + e^{\pm\frac{i2\pi}{3}}|XZ\rangle + e^{\pm\frac{i4\pi}{3}}|YZ\rangle). \quad (4)$$

We select the projected Wannier orbitals by focusing exclusively on the Fe $3d$–S $3p$ hybrid orbitals near the Fermi level. This approach inherently encompasses both the indirect d-p-d hoppings and the direct d-d ones. Figures S2 and S3 in SM [39] display the comparison between DFT and Wannier-interpolated band structures of the $FePS_3$ monolayer, showing that the chosen MLWFs accurately reproduce the *ab initio* electronic states. With these Wannier functions, we can obtain the hopping parameters of different ions and orbitals.

We first examine the major hopping channels associated with the 1NN FM coupling in $FePS_3$ monolayer. In Table II, we list the hopping parameters and note that the XY orbitals

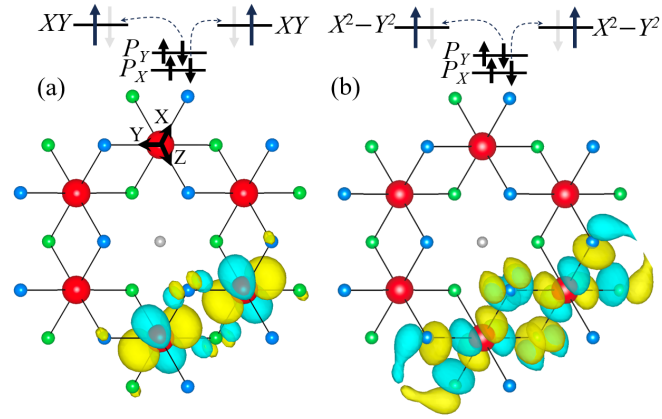

FIG. 6. Schematic plot of the 1NN FM superexchange and some associated hopping channels in $FePS_3$ monolayer represented by Wannier orbitals: the superexchange (a) via (XY)-(p_X, p_Y)-(XY) orbitals, and (b) via (X^2-Y^2)-(p_X, p_Y)-(X^2–Y^2).

of Fe_0-Fe_1 ions show the largest hopping integral of 277 meV. Other hopping integrals are smaller than one-third of that value. To understand why there is such a large hopping integral between the two XY orbitals, we illustrate the real-space distribution of the XY-like MLWFs in Fig. 6(a). In the edge-sharing octahedra, the XY orbitals on adjacent Fe sites are directed toward each other. Considering the 1NN distance of 3.42 Å, this leads to $dd\sigma$ hybridization. Moreover, as seen in Fig. 6(a), aside from the direct hopping integral, the XY orbitals can interact through the indirect hoppings via sulfur $3p$ orbitals, which is evident from the $pd\pi$ hybridization through the (p_X, p_Y) orbitals. In total, between adjacent XY orbitals, there are not only direct hopping integrals but also indirect ones through the ligands, thus resulting in the largest hopping parameter. Then, we illustrate all hopping integrals exceeding 50 meV, as seen in Fig. 6 and S4 in SM [39]. We find that the direct d-d hoppings are relatively small, while the indirect ones via ligands play a major role. For example, the superexchange channel involving (X^2-Y^2)-(p_X, p_Y)-(X^2-Y^2) primarily arises from $pd\sigma$ hybridization via the (p_X, p_Y) orbitals, as seen in Fig. 6(b). Considering virtual charge fluctuations, local Hund exchange, and the Pauli exclusion principle, those superexchange channels yield an FM coupling. Such near 90° 1NN superexchange channels leading to the FM J_1 have also been confirmed in other 2D FM semiconductors such as CrI_3 [11–13] and $Cr_2Ge_2Te_6$ [13].

As shown in Table II, the hopping parameters for 2NN Fe_0-Fe_2 are much smaller, aligning with our DFT calculations of small $J_2 = -0.34$ meV. Specifically, the most significant hopping integral for 2NN, arising from the indirect d-p-d hopping, is 54 meV between the XZ and X^2-Y^2 orbitals, as shown in Fig. S5 in SM [39]. The hopping between these two orbitals is solely mediated by a p_Y orbital, resulting in a much weaker hybridization. All other hopping integrals are smaller and thus all their contributions to the J_2 are quite limited.

By looking at the even smaller 4NN Fe_0-Fe_4 hoppings, their contributions to the 4NN superexchange should be negligibly weak. To obtain the J_4 exchange parameter, we additionally calculated a double-stripe AF magnetic structure, as seen in Fig S6 in SM [39]. We then find that J_4 is only

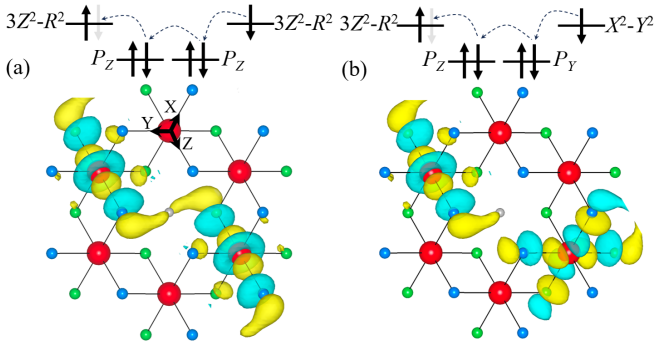

FIG. 7. Schematic plot of the 3NN AF superexchange and some associated hopping channels in $FePS_3$ monolayer represented by Wannier orbitals: the long-range superexchange (a) via ($3Z^2$-R^2)-(p_Z)-(p_Z)-($3Z^2$-R^2) orbitals, and (b) via ($3Z^2$-R^2)-(p_Z)-(p_Y)-(X^2-Y^2).

−0.04 meV and, therefore, the tiny 4NN superexchange is of no more concern in this work.

Notably, for 3NN Fe_0-Fe_3, the large distance of 6.84 Å is twice that of 1NN and thereby renders the direct d-d hopping negligible. However, as seen in Table II, the hopping integral between the $3Z^2$-R^2 orbitals is 140 meV, and the integral between $3Z^2$-R^2 and X^2-Y^2 is 99 meV, both of which are significantly larger than most of the 1NN hopping parameters. Therefore, it is crucial to investigate how these d orbitals via ligands facilitate such large hoppings and then contribute to the strong long-range superexchange interactions. To illustrate the superexchange channels, we depict the real-space distribution of the $3Z^2$-R^2 and X^2-Y^2-like MLWFs in Fig. 7. Our results indicate that the $3Z^2$-R^2 orbitals of Fe_0 and Fe_3 ions engage in long-range superexchange via p_Z orbitals of two sulfur ions. Each $3Z^2$-R^2 orbital forms a strong $pd\sigma$ hybridization with the adjacent sulfur p_Z orbitals. Additionally, there is a hybridization between the two sulfur p_Z orbitals mediated by the intermediate P atoms. This long-range hopping channel notably increases the hopping integral between the two $3Z^2$-R^2 orbitals. Similarly, the $3Z^2$-R^2 and X^2-Y^2 orbitals form a long-range hopping through two sulfur ions, facilitated by their respective $pd\sigma$ hybridizations with the p_Z and p_Y orbitals. The p_Z and p_Y orbitals on the same plane create a 90° head-to-head ($\frac{1}{2}\,pp\sigma - \frac{1}{2}\,pp\pi$) hybridization. Our results reveal that the effective hopping integral for the $3Z^2$-R^2 and X^2-Y^2 orbitals is smaller than the hopping integral between two $3Z^2$-R^2 orbitals, but these values are significantly larger than most of the 1NN hopping integrals. Considering the $3d^{5\uparrow}L^{1\downarrow}_{z^2}$ ground state, in which both the majority-spin $3Z^2$-R^2 and X^2-Y^2 orbitals are fully occupied by electrons, the above long-range superexchange channels consequently contribute to the strong J_3 AF coupling.

To summarize, our calculations confirm the zigzag AF ground state of $FePS_3$ monolayer, and find the competitive 1NN FM J_1 and 3NN AF J_3 but the much weaker 2NN AF J_2 and the negligibly weak 4NN AF J_4. In combination with Wannier function analyses and the derived hopping parameters, we find that the 1NN FM J_1 is primarily attributed to near 90° superexchange interactions associated with several channels. The strong 3NN AF J_3 arises from long-range superexchange interactions through two major channels: one is between two $3Z^2$-R^2 orbitals via the p_Z orbitals of two sulfur ions (mediated by the intermediate P atoms) and their $pd\sigma$ hybridizations as shown in Fig. 7(a); the other involves $3Z^2$-R^2 and X^2-Y^2 orbitals via the S p_Z–S p_Y channel and their respective $pd\sigma$ hybridizations as shown in Fig. 7(b). It is the competitive 1NN FM J_1 and 3NN AF J_3 that determine the zigzag AFM of $FePS_3$ monolayer.

D. The T_N and strain effect

To estimate the T_N of $FePS_3$ monolayer, we assume a spin Hamiltonian and carry out PTMC simulations

$$H = -\sum_{k=1,2,3}\sum_{i,j}\frac{J_k}{2}\mathbf{S}_i\cdot\mathbf{S}_j - \sum_i D\left(S_i^z\right)^2. \tag{5}$$

The first term represents the isotropic Heisenberg exchange, and the sum runs over all Fe^{2+} sites i with $S = 2$ in the spin lattice, and j runs over the kNN Fe^{2+} sites of each i with their respective magnetic couplings J_k given as $J_1 = 3.13$ meV, $J_2 = -0.34$ meV, and $J_3 = -2.01$ meV (FM when $J > 0$). The second term describes the MA with $S^z = 2$ (easy

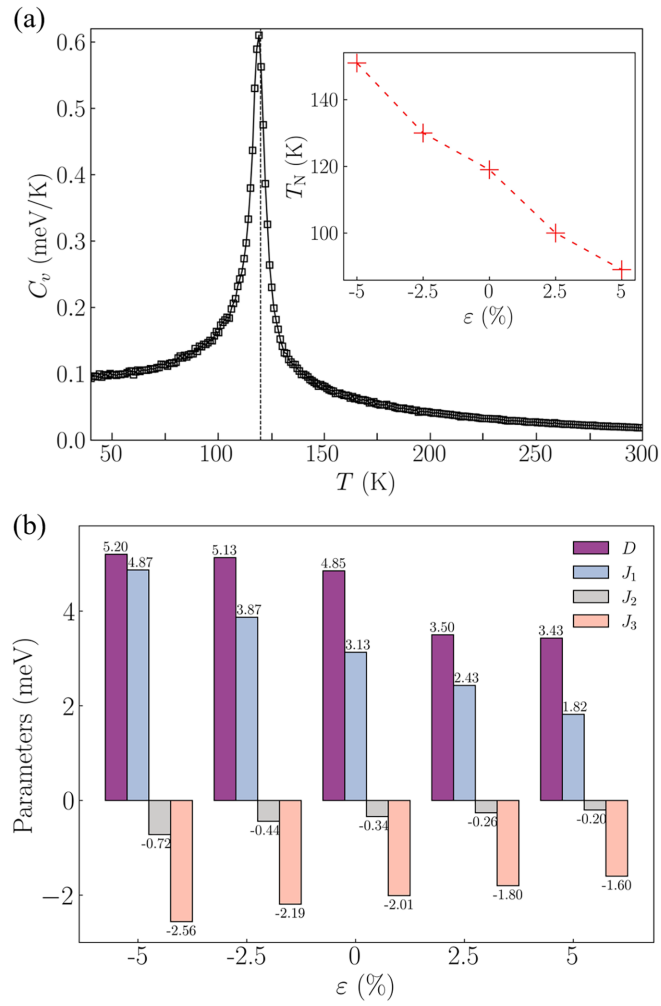

FIG. 8. (a) PTMC simulations of the magnetic specific heat of $FePS_3$ monolayer. The inset shows the increasing T_N under compressive strains. (b) The MA value D and exchange parameters J_1, J_2, and J_3 (meV) of $FePS_3$ monolayer under the strains.

perpendicular magnetization when $D > 0$). Given the giant SIA of 19.4 meV/Fe for the $3d^5\uparrow L_{z+}^{1\downarrow}$ ground state, we obtain $D = 4.85$ meV. Employing these exchange parameters and the huge MA value, our PTMC simulations yield $T_N = 119$ K for $FePS_3$ monolayer as seen in Fig. 8(a), and this agrees well with the experimental $T_N = 118$ K [24,28,29].

Strain is widely used to tune the properties of 2D materials [50,51]. Here we investigate a possible impact of a biaxial strain on $FePS_3$ monolayer. Our calculations show that under strain, $FePS_3$ monolayer remains in the robust $3d^5\uparrow L_{z+}^{1\downarrow}$ ground state. In particular, the compressive strains enhance the exchange parameters J_k ($k = 1$–3) and the MA value D, and thus boost T_N to 151 K under a -5% compressive strain, as seen in Fig. 8.

E. $FePSe_3$ monolayer: Ising zigzag AFM

Bulk $FePSe_3$ is a zigzag AF semiconductor with $T_N = 119$ K [23], and it has the same crystal structure as bulk $FePS_3$. $FePSe_3$ monolayer has not yet been experimentally synthesized to date. Here we also study the electronic structure and magnetism of $FePSe_3$ monolayer to check whether it is an Ising magnet too.

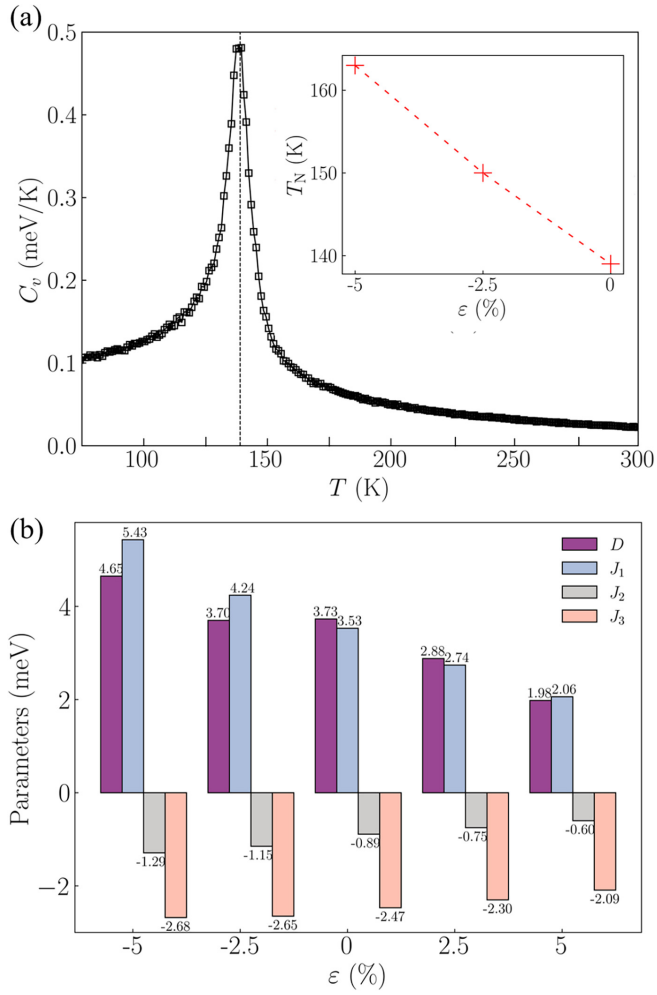

FIG. 9. (a) PTMC simulations of the magnetic specific heat of $FePSe_3$ monolayer. The inset shows the increasing T_N under compressive strains. (b) The MA value D and exchange parameters J_1, J_2, and J_3 (meV) of $FePSe_3$ monolayer under the strains.

Our results indicate that $FePSe_3$ monolayer is in the same $3d^5\uparrow L_{z+}^{1\downarrow}$ ground state as $FePS_3$ monolayer, by a direct comparison of different spin-orbital states, as seen in Figs. 4 and S7 in SM [39]. It has the spin moment of 3.46 μ_B in the FM state and the orbital moment of 0.66 μ_B along the z axis (see Table I). Both values are smaller than the corresponding ones of 3.55 μ_B and 0.73 μ_B in $FePS_3$ monolayer, and this is due to the stronger Fe-Se covalence reduction in $FePSe_3$. This is also in line with the experimental observations that bulk $FePSe_3$ has a smaller effective magnetic moment than bulk $FePS_3$ [23,27]. Moreover, through our results in Fig. 4 and following the same procedures as in Sec. III B, we estimate the SOC parameter $\zeta = 52$ meV, and the trigonal crystal field splitting of 123 meV between the higher a_{1g} singlet and lower e_g^π doublet both out of the octahedral t_{2g} triplet. The nice agreement with the typical Fe^{2+} ζ parameter of 50–60 meV once again reflects the good accuracy of our calculations. The a_{1g}-e_g^π splitting turns out to be much larger than the SOC parameter, and this enables us to restrict our discussion of the SOC effect within the half-filled minority-spin e_g^π doublet. As $FePSe_3$ monolayer has a large orbital moment along the z axis, which fixes via the SOC the spin orientation also along the z axis, a tentative rotation of the spin moment into the xy plane would cost a lot of the SOC energy. Indeed, our calculations find that the perpendicular MAE is 14.9 meV/Fe in $FePSe_3$ (see Fig. 4), which arises from the huge SIA associated with the $3d^5\uparrow L_{z+}^{1\downarrow}$ ground state. Then, $FePSe_3$ monolayer is indeed an Ising magnet too.

By comparing four magnetic structures (Fig. 5) in our calculations, we find that $FePSe_3$ monolayer is a zigzag AF semiconductor with a band gap of 0.6 eV. The calculated exchange parameters are $J_1 = 3.53$ meV, $J_2 = -0.89$ meV, and $J_3 = -2.47$ meV, as seen in Table I. We also calculate the hopping parameters for $FePSe_3$ monolayer using Wannier functions, as seen in Table III. These hopping parameters have the same tendency as those in $FePS_3$ monolayer (see Table II for a comparison): the big 1NN and 3NN ones but much smaller 2NN and negligible 4NN, and they could help us to understand the competitive 1NN FM and 3NN AF but relatively weak 2NN AF and the negligible 4NN one, following the above discussion in Sec. III C. Note that the stronger Fe $3d$-Se $4p$ hybridizations, counteracting the increasing atomic distances in $FePSe_3$ normally with decreasing hopping integrals, give rise to quite similar hopping integrals t's for $FePSe_3$ as in $FePS_3$ (see Tables II and III). Then, together with the reduced Hubbard U, the superexchange parameters (roughly in the scale of t^2/U) seem larger in $FePSe_3$ than in $FePS_3$, as seen in Table I. Then, using Eq. (5), the aforementioned three exchange parameters and the MAE parameter for $FePSe_3$ monolayer, our PTMC simulations yield $T_N = 140$ K, and the T_N could be increased up to 163 K under the -5% compressive strain (see Fig. 9).

Note that the $T_N = 140$ K for bare $FePSe_3$ monolayer seems overestimated, compared with the experimental $T_N = 119$ K for bulk $FePSe_3$ [23]. This is associated with the likely overestimated exchange parameters due to the calculated smaller Hubbard $U = 2.7$ eV from the constrained random

TABLE III. The hopping parameters (meV) of 1NN Fe_0-Fe_1, 2NN Fe_0-Fe_2, 3NN Fe_0-Fe_3, and 4NN Fe_0-Fe_4 in $FePSe_3$ monolayer.

Hopping (t)		Fe_0				
		$3Z^2$-R^2	X^2-Y^2	XY	XZ	YZ
Fe_1	$3Z^2$-R^2	–62	0	105	7	5
	X^2-Y^2	0	–45	0	33	–32
	XY	105	0	–229	23	23
	XZ	7	33	23	68	–45
	YZ	5	–32	23	–45	68
Fe_2	$3Z^2$-R^2	5	18	3	–31	13
	X^2-Y^2	15	25	34	–36	–12
	XY	–17	6	17	–9	–23
	XZ	–16	–45	16	–2	–10
	YZ	28	19	–19	16	17
Fe_3	$3Z^2$-R^2	128	96	2	3	–30
	X^2-Y^2	96	18	–5	–5	52
	XY	2	–5	5	–12	–1
	XZ	3	–5	–12	5	0
	YZ	–30	52	–1	0	–40
Fe_4	$3Z^2$-R^2	12	4	2	–6	5
	X^2-Y^2	4	2	2	–8	7
	XY	2	2	5	–2	–2
	XZ	–6	–8	–2	–3	10
	YZ	5	7	–2	10	5

phase approximation. When we choose the common value of $U = 4.0$ eV in our GGA + SOC + U calculations, the T_N is estimated to be 99 K for $FePSe_3$ monolayer (105 K for $FePS_3$ monolayer) (see the results in Table S2 and Fig. S1 in SM [39]). Note, however, that the Ising-type zigzag AF semiconducting ground state with the $3d^{5\uparrow}L_{z+}^{1\downarrow}$ spin-orbital state remains unchanged at all. The present results and prediction call for an experimental study on $FePSe_3$ monolayer.

IV. CONCLUSION

To conclude, we study the electronic structure and magnetism of $FePS_3$ and $FePSe_3$ monolayers using density functional calculations, crystal field level diagrams, Wannier function analyses, and PTMC simulations. We find that both materials are in the robust Fe^{2+} $3d^{5\uparrow}L_{z+}^{1\downarrow}$ ground state with the formal $S_z = 2$ and $L_z = 1$. The large orbital moment produces a significant SIA and thus determines the Ising magnetism. The derived hopping parameters from Wannier functions help to explain the competitive 1NN FM and 3NN AF couplings but relatively weaker 2NN AF coupling, all of which determine the zigzag AFM. Our PTMC simulations well reproduce the experimental $T_N = 118$ K for $FePS_3$ monolayer and predict a close or even higher T_N for $FePSe_3$ monolayer, and moreover, their T_N could be enhanced under a compressive strain. This study provides an insight into the Ising-type zigzag AFM of $FePS_3$ and $FePSe_3$ monolayers.

ACKNOWLEDGMENTS

This work was supported by National Natural Science Foundation of China (Grants No. 12104307, No. 12174062, and No. 12241402) and by Innovation Program for Quantum Science and Technology.

[1] K. S. Novoselov, A. K. Geim, S. V. Morozov, D. Jiang, Y. Zhang, S. V. Dubonos, I. V. Grigorieva, and A. A. Firsov, Electric field effect in atomically thin carbon films, Science **306**, 666 (2004).

[2] A. K. Geim and K. S. Novoselov, The rise of graphene, Nat. Mater. **6**, 183 (2007).

[3] T. Li, S. Jiang, N. Sivadas, Z. Wang, Y. Xu, D. Weber, J. E. Goldberger, K. Watanabe, T. Taniguchi, C. J. Fennie, K. F. Mak, and J. Shen, Pressure-controlled interlayer magnetism in atomically thin CrI_3, Nat. Mater. **18**, 1303 (2019).

[4] T. Song, Z. Fei, M. Yankowitz, Z. Lin, Q. Jiang, K. Hwangbo, Q. Zhang, B. Sun, T. Taniguchi, K. Watanabe, M. A. McGuire, D. Graf, T. Cao, J.-H. Chu, D. H. Cobden, C. R. Dean, D. Xiao, and X. Xu, Switching 2D magnetic states via pressure tuning of layer stacking, Nat. Mater. **18**, 1298 (2019).

[5] J. Li, X. Yang, Y. Liu, B. Huang, R. Wu, Z. Zhang, B. Zhao, H. Ma, W. Dang, Z. Wei, K. Wang, Z. Lin, X. Yan, M. Sun, B. Li, X. Pan, J. Luo, G. Zhang, Y. Liu, Y. Huang *et al.*, General synthesis of two-dimensional van der Waals heterostructure arrays, Nature (London) **579**, 368 (2020).

[6] K. S. Burch, D. Mandrus, and J.-G. Park, Magnetism in two-dimensional van der Waals materials, Nature (London) **563**, 47 (2018).

[7] T. Song, X. Cai, M. W.-Y. Tu, X. Zhang, B. Huang, N. P. Wilson, K. L. Seyler, L. Zhu, T. Taniguchi, K. Watanabe, M. A. McGuire, D. H. Cobden, D. Xiao, W. Yao, and X. Xu, Giant tunneling magnetoresistance in spin-filter van der Waals heterostructures, Science **360**, 1214 (2018).

[8] B. Huang, G. Clark, E. Navarro-Moratalla, D. R. Klein, R. Cheng, K. L. Seyler, D. Zhong, E. Schmidgall, M. A. McGuire, D. H. Cobden, W. Yao, D. Xiao, P. Jarillo-Herrero, and X. Xu, Layer-dependent ferromagnetism in a van der Waals crystal down to the monolayer limit, Nature (London) **546**, 270 (2017).

[9] C. Gong, L. Li, Z. Li, H. Ji, A. Stern, Y. Xia, T. Cao, W. Bao, C. Wang, Y. Wang, Z. Q. Qiu, R. J. Cava, S. G. Louie, J. Xia, and X. Zhang, Discovery of intrinsic ferromagnetism in two-dimensional van der Waals crystals, Nature (London) **546**, 265 (2017).

[10] N. D. Mermin and H. Wagner, Absence of ferromagnetism or antiferromagnetism in one- or two-dimensional isotropic Heisenberg models, Phys. Rev. Lett. **17**, 1133 (1966).

[11] H. Wang, F. Fan, S. Zhu, and H. Wu, Doping enhanced ferromagnetism and induced half-metallicity in CrI_3 monolayer, Europhys. Lett. **114**, 47001 (2016).

[12] J. L. Lado and J. Fernández-Rossier, On the origin of magnetic anisotropy in two dimensional CrI_3, 2D Mater. **4**, 035002 (2017).

[13] C. Xu, J. Feng, H. Xiang, and L. Bellaiche, Interplay between Kitaev interaction and single ion anisotropy in ferromagnetic

CrI_3 and $CrGeTe_3$ monolayers, npj Comput. Mater. **4**, 57 (2018).

[14] D.-H. Kim, K. Kim, K.-T. Ko, J.-H. Seo, J. S. Kim, T.-H. Jang, Y. Kim, J.-Y. Kim, S.-W. Cheong, and J.-H. Park, Giant magnetic anisotropy induced by ligand *LS* coupling in layered Cr compounds, Phys. Rev. Lett. **122**, 207201 (2019).

[15] K. Yang, F. Fan, H. Wang, D. I. Khomskii, and H. Wu, VI_3: A two-dimensional Ising ferromagnet, Phys. Rev. B **101**, 100402(R) (2020).

[16] G.-D. Zhao, X. Liu, T. Hu, F. Jia, Y. Cui, W. Wu, M.-H. Whangbo, and W. Ren, Difference in magnetic anisotropy of the ferromagnetic monolayers VI_3 and CrI_3, Phys. Rev. B **103**, 014438 (2021).

[17] A. De Vita, T. T. P. Nguyen, R. Sant, G. M. Pierantozzi, D. Amoroso, C. Bigi, V. Polewczyk, G. Vinai, L. T. Nguyen, T. Kong, J. Fujii, I. Vobornik, N. B. Brookes, G. Rossi, R. J. Cava, F. Mazzola, K. Yamauchi, S. Picozzi, and G. Panaccione, Influence of orbital character on the ground state electronic properties in the van der Waals transition metal iodides VI_3 and CrI_3, Nano Lett. **22**, 7034 (2022).

[18] Z. Lin, B. Huang, K. Hwangbo, Q. Jiang, Q. Zhang, Z. Liu, Z. Fei, H. Lv, A. Millis, M. McGuire, D. Xiao, J.-H. Chu, and X. Xu, Magnetism and its structural coupling effects in 2D Ising ferromagnetic insulator VI_3, Nano Lett. **21**, 9180 (2021).

[19] D. Hovančík, J. Pospisil, K. Carva, V. Sechovsky, and C. Piamonteze, Large orbital magnetic moment in VI_3, Nano Lett. **23**, 1175 (2023).

[20] M. Gibertini, M. Koperski, A. F. Morpurgo, and K. S. Novoselov, Magnetic 2D materials and heterostructures, Nat. Nanotechnol. **14**, 408 (2019).

[21] K. F. Mak, J. Shan, and D. C. Ralph, Probing and controlling magnetic states in 2D layered magnetic materials, Nat. Rev. Phys. **1**, 646 (2019).

[22] C. Gong and X. Zhang, Two-dimensional magnetic crystals and emergent heterostructure devices, Science **363**, eaav4450 (2019).

[23] A. Wiedenmann, J. Rossat-Mignod, A. Louisy, R. Brec, and J. Rouxel, Neutron diffraction study of the layered compounds $MnPSe_3$ and $FePSe_3$, Solid State Commun. **40**, 1067 (1981).

[24] J.-U. Lee, S. Lee, J. H. Ryoo, S. Kang, T. Y. Kim, P. Kim, C.-H. Park, J.-G. Park, and H. Cheong, Ising-type magnetic ordering in atomically thin $FePS_3$, Nano Lett. **16**, 7433 (2016).

[25] M. J. Coak, D. M. Jarvis, H. Hamidov, C. R. S. Haines, P. L. Alireza, C. Liu, S. Son, I. Hwang, G. I. Lampronti, D. Daisenberger, P. Nahai-Williamson, A. R. Wildes, S. S. Saxena, and J.-G. Park, Tuning dimensionality in van-der-Waals antiferromagnetic Mott insulators $TMPS_3$, J. Phys.: Condens. Matter **32**, 124003 (2020).

[26] Y. Zheng, X.-X. Jiang, X.-X. Xue, J. Dai, and Y. Feng, *Ab initio* study of pressure-driven phase transition in $FePS_3$ and $FePSe_3$, Phys. Rev. B **100**, 174102 (2019).

[27] P. A. Joy and S. Vasudevan, Magnetism in the layered transition-metal thiophosphates MPS_3 (M = Mn, Fe, and Ni), Phys. Rev. B **46**, 5425 (1992).

[28] Q. Zhang, K. Hwangbo, C. Wang, Q. Jiang, J.-H. Chu, H. Wen, D. Xiao, and X. Xu, Observation of giant optical linear dichroism in a zigzag antiferromagnet $FePS_3$, Nano Lett. **21**, 6938 (2021).

[29] X. Wang, K. Du, Y. Y. F. Liu, P. Hu, J. Zhang, Q. Zhang, M. H. S. Owen, X. Lu, C. K. Gan, P. Sengupta, C. Kloc, and Q. Xiong, Raman spectroscopy of atomically thin two-dimensional magnetic iron phosphorus trisulfide ($FePS_3$) crystals, 2D Mater. **3**, 031009 (2016).

[30] B. L. Chittari, Y. Park, D. Lee, M. Han, A. H. MacDonald, E. Hwang, and J. Jung, Electronic and magnetic properties of single-layer MPX_3 metal phosphorous trichalcogenides, Phys. Rev. B **94**, 184428 (2016).

[31] T. Olsen, Magnetic anisotropy and exchange interactions of two-dimensional $FePS_3$, $NiPS_3$ and $MnPS_3$ from first principles calculations, J. Phys. D: Appl. Phys. **54**, 314001 (2021).

[32] J.-m. Zhang, Y.-z. Nie, X.-g. Wang, Q.-l. Xia, and G.-h. Guo, Strain modulation of magnetic properties of monolayer and bilayer $FePS_3$ antiferromagnet, J. Magn. Magn. Mater. **525**, 167687 (2021).

[33] T. Y. Kim and C.-H. Park, Magnetic anisotropy and magnetic ordering of transition-metal phosphorus trisulfides, Nano Lett. **21**, 10114 (2021).

[34] M. Amirabbasi and P. Kratzer, Orbital and magnetic ordering in single-layer $FePS_3$: A DFT $+U$ study, Phys. Rev. B **107**, 024401 (2023).

[35] P. Li, X. Li, J. Feng, J. Ni, Z.-X. Guo, and H. Xiang, Origin of zigzag antiferromagnetic order in XPS_3 (X = Fe, Ni) monolayers, Phys. Rev. B **109**, 214418 (2024).

[36] G. Kresse and J. Hafner, *Ab initio* molecular dynamics for liquid metals, Phys. Rev. B **47**, 558 (1993).

[37] J. P. Perdew, K. Burke, and M. Ernzerhof, Generalized gradient approximation made simple, Phys. Rev. Lett. **77**, 3865 (1996).

[38] G. Ouvrard, R. Brec, and J. Rouxel, Structural determination of some MPS_3 layered phases (M = Mn, Fe, Co, Ni and Cd), Mater. Res. Bull. **20**, 1181 (1985).

[39] See Supplemental Material at http://link.aps.org/supplemental/10.1103/PhysRevB.110.024427 for the convergence tests, the tested $U = 4$ eV results for $FePS_3$ and $FePSe_3$ monolayers, the 1NN and 2NN hopping channels, and the DOS results of $FePSe_3$ monolayer.

[40] V. I. Anisimov, F. Aryasetiawan, and A. I. Lichtenstein, First-principles calculations of the electronic structure and spectra of strongly correlated systems: the LDA $+U$ method, J. Phys.: Condens. Matter **9**, 767 (1997).

[41] L. Vaugier, H. Jiang, and S. Biermann, Hubbard U and Hund exchange J in transition metal oxides: Screening versus localization trends from constrained random phase approximation, Phys. Rev. B **86**, 165105 (2012).

[42] D. I. Khomskii, *Transition Metal Compounds* (Cambridge University Press, Cambridge, 2014).

[43] J. P. Allen and G. W. Watson, Occupation matrix control of d- and f-electron localisations using DFT $+U$, Phys. Chem. Chem. Phys. **16**, 21016 (2014).

[44] A. A. Mostofi, J. R. Yates, Y.-S. Lee, I. Souza, D. Vanderbilt, and N. Marzari, wannier90: A tool for obtaining maximally-localised Wannier functions, Comput. Phys. Commun. **178**, 685 (2008).

[45] N. Marzari, A. A. Mostofi, J. R. Yates, I. Souza, and D. Vanderbilt, Maximally localized Wannier functions: Theory and applications, Rev. Mod. Phys. **84**, 1419 (2012).

[46] K. Hukushima and K. Nemoto, Exchange Monte Carlo method and application to spin glass simulations, J. Phys. Soc. Jpn. **65**, 1604 (1996).

[47] N. Metropolis and S. Ulam, The Monte Carlo method, J. Am. Stat. Assoc. **44**, 335 (1949).

[48] F. Mertens, D. Mönkebüscher, U. Parlak, C. Boix-Constant, S. Mañas-Valero, M. Matzer, R. Adhikari, A. Bonanni, E. Coronado, A. M. Kalashnikova, D. Bossini, and M. Cinchetti, Ultrafast coherent THz lattice dynamics coupled to spins in the van der waals antiferromagnet $FePS_3$, Adv. Mater. **35**, 2208355 (2023).

[49] D. Lançon, H. C. Walker, E. Ressouche, B. Ouladdiaf, K. C. Rule, G. J. McIntyre, T. J. Hicks, H. M. Rønnow, and A. R. Wildes, Magnetic structure and magnon dynamics of the quasi-two-dimensional antiferromagnet $FePS_3$, Phys. Rev. B **94**, 214407 (2016).

[50] J. Cenker, S. Sivakumar, K. Xie, A. Miller, P. Thijssen, Z. Liu, A. Dismukes, J. Fonseca, E. Anderson, X. Zhu, X. Roy, D. Xiao, J.-H. Chu, T. Cao, and X. Xu, Reversible strain-induced magnetic phase transition in a van der Waals magnet, Nat. Nanotechnol. **17**, 256 (2022).

[51] Y. Wang, C. Wang, S.-J. Liang, Z. Ma, K. Xu, X. Liu, L. Zhang, A. S. Admasu, S.-W. Cheong, L. Wang, M. Chen, Z. Liu, B. Cheng, W. Ji, and F. Miao, Strain-sensitive magnetization reversal of a van der Waals magnet, Adv. Mater. **32**, 2004533 (2020).